Materials and Design 174 (2019) 107792

Contents lists available at ScienceDirect

Materials and Design

journal homepage: www.elsevier.com/locate/matdes

# Effect of preheating on the thermal, microstructural and mechanical properties of selective electron beam melted Ti-6Al-4V components

Chu Lun Alex Leung [a,b,*], Riccardo Tosi [c], Emmanuel Muzangaza [c], Sara Nonni [b,d], Philip J. Withers [d], Peter D. Lee [a,b,*]

[a] Department of Mechanical Engineering, University College London, Torrington Place, London WC1E 7JE, UK
[b] Research Complex at Harwell, Rutherford Appleton Laboratory, Harwell, Oxfordshire, Oxon OX11 0FA, UK
[c] The Manufacturing Technology Centre, Antsy Park, Coventry CV7 9JU, UK
[d] Henry Royce Institute, School of Materials, University of Manchester, Oxford Road, Manchester, M13 9PL, UK

## HIGHLIGHTS

- Preheating in selective electron beam melting affects properties of the powder bed and additive manufacturing (AM) parts.
- X-ray computed tomography and image-based modelling were used to evaluate properties of the powder bed and AM parts in 3D.
- The preheated powder bed has an anisotropic microstructure, exhibiting a low thermal conductivity along its build direction.
- High preheating has a minimal effect on part density but it decreases the build accuracy and microhardness of the AM parts.

## GRAPHICAL ABSTRACT

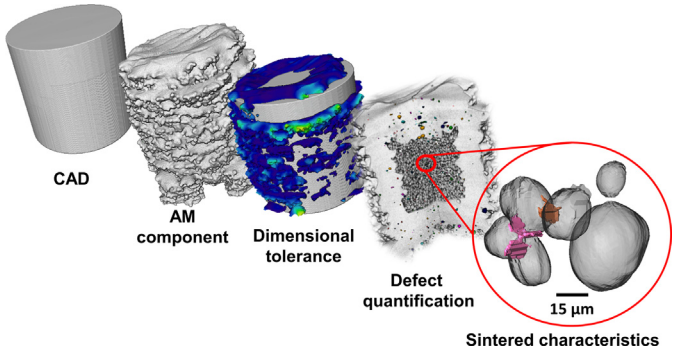


## ARTICLE INFO

*Article history:*
Received 18 February 2019
Received in revised form 28 March 2019
Accepted 9 April 2019
Available online 12 April 2019

*Keywords:*
Preheating
Thermal conductivity
Additive manufacturing
Dimensional accuracy
X-ray computed tomography (CT)
Image-based modelling

## ABSTRACT

Two-stage preheating is used in selective electron beam melting (SEBM) to prevent powder spreading during additive manufacturing (AM); however, its effects on part properties have not been widely investigated. Here, we employed three different preheat treatments (energy per unit area, $E_A$) to a Ti-6Al-4V powder bed. Each standalone build, we fabricated a large block sample and seven can-shaped samples containing sintered powder. X-ray computed tomography (XCT) was employed to quantify the porosity and build accuracy of the can-shaped samples. The effective thermal conductivity of the sintered powder bed was estimated by XCT image-based modelling. The microstructural and mechanical properties of the block sample were examined by scanning electron microscopy and microhardness testing, respectively. The results demonstrate that increasing $E_A$ reduces the anisotropy of tortuosity and increases the thermal conductivity of the sintered powder bed, improving the heat transfer efficiency for subsequent beam-matter interaction. High preheat has a negligible effect on the porosity of large AM components; however, it decreases the microhardness from 330 ± 7 to 315 ± 11 HV0.5 and increases the maximum build error from 330 to 400 μm. Our study shows that a medium $E_A$ (411 kJ m$^{-2}$) is sufficient to produce components with a high hardness whilst optimising build accuracy.



* Corresponding authors at: Department of Mechanical Engineering, University College London, Torrington Place, London WC1E 7JE, UK.
*E-mail addresses:* alex.leung@ucl.ac.uk (C.L.A. Leung), peter.lee@ucl.ac.uk (P.D. Lee).

https://doi.org/10.1016/j.matdes.2019.107792

## 1. Introduction

Ti-6Al-4V is widely used in the aerospace and biomedical sectors owing to its high strength to weight ratio, excellent corrosion resistance, and biocompatibility [1]. However, Ti-based alloys are generally difficult to machine owing to their low thermal conductivity and high hardness at elevated temperature, leading to high tool wear and hence expensive machining [2]. Powder bed fusion (PBF) additive manufacturing (AM) technologies, such as selective electron beam melting (SEBM), fuse powder particles together using a focused heat source to build a near-net shaped component, layer by layer, directly from a computer-generated model [3,4], reducing the need of machining.

In AM, build components are subjected to a rapid heating and cooling cycle, with a high thermal gradient along their build direction, they partially result in high residual stresses [5], distortion, and poor dimensional accuracy [6]. These components may also exhibit undesired build features, *e.g.* porosity [7] and spatter [8,9] owing to the complex beam-matter interaction [10], powder oxidation [11] and melt flow behaviour [12]; an anisotropic microstructure due to rapid solidification [13]; and high surface roughness [14,15], impairing their fatigue performance [16] and preventing the adoption of AM technologies for safety-critical components. Understanding the relationship between the AM process and resultant part properties is crucial for process and product optimisation.

In SEBM, the beam energy is mainly controlled by adjusting the beam current applied to the electron gun under high vacuum ($10^{-1}$–$10^{-3}$ Pa) and the beam focus is adjusted by magnetic coils. For the Arcam EBM process, the machine first lowers its build platform, next it spreads the powder on the build platform, it then applies a default two-stage preheat (referred to as preheat 1 and 2) by scanning across the powder bed first with a low power density electron beam which is controlled by the beam current, scan rate, and beam focus [17], and then uses a focused beam for subsequent melting. [18,19].

The main purpose of preheating is to prevent build failure caused by charging of electrons, commonly referred to as "smoke" among SEBM users, it is also known as powder spreading [20–23], powder pushing [24] or powder blowing. Previous studies show preheating can increase the effective mechanical strength [17,25], electrical, and thermal conductivity ($\lambda_{eff}$) [19,26] of the sintered powder, improving the beam-matter interaction efficiency [27], and hence a lower beam current can be used for subsequent melt scans. [21] It also reduces the formation of balling [17,28] and lowers the thermal gradient during melting, reducing distortion, warpage, and in-built residual stresses in AM components [19,20,29]. Sigl et al. [22] identified three disadvantages of preheating:

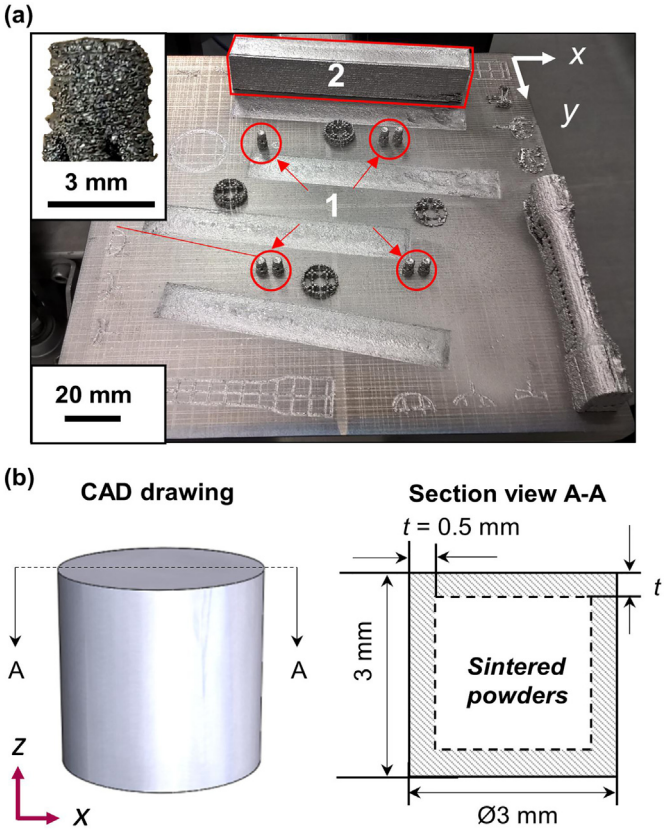


**Fig. 2.** SEBM samples showing: (a) 7 can-shaped samples (a side-view inset shows an example of a high-preheat can-shaped sample) and a block sample, and (b) a CAD drawing and a *X-Z* cross-sectional view of the can-shaped sample. Note: *X*/*Y* is the lateral direction and *Z* is the build direction.

(1) it increases the overall build time and energy consumption; (2), it requires an extra post-processing step to remove the lightly sintered particles, and (3) it may limit the detail of the build features because the lightly sintered particles are difficult to remove in complex internal geometries. All three disadvantages can be effectively controlled by employing a suitable preheating strategy, which has been overlooked in the literature.

To date, there have been no comprehensive studies of preheating effects on the build quality of SEBM components, including the dimensional accuracy, resultant microstructures (*e.g.* defects), and mechanical

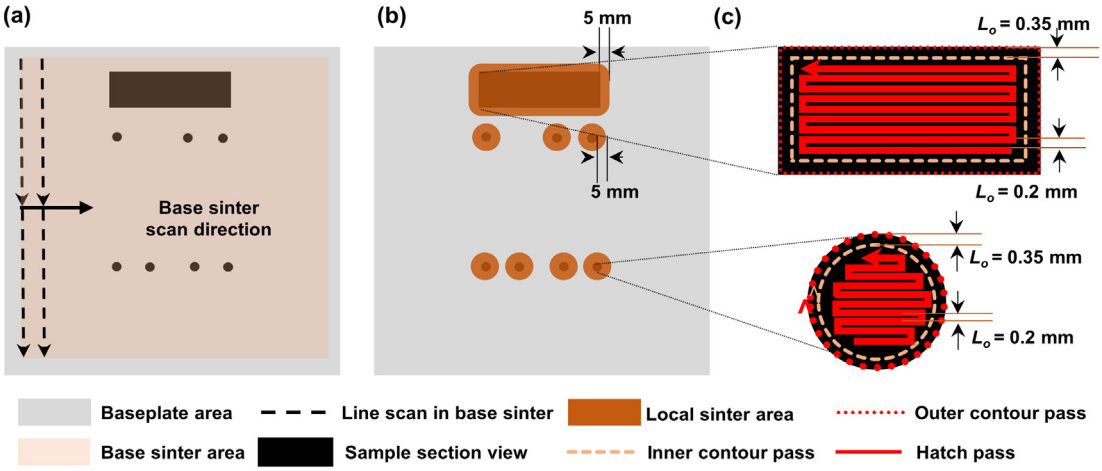


**Fig. 1.** Top view schematic of the SEBM build chamber showing the preheating and melting stages: (a) base sinter - the electron beam rasters across the entire powder bed, (b) local sinter – the electron beam sinters the area of the sample section region plus a region of 5 mm from its boundary, and (c) melting - the electron beam melts the boundary of the sample section using 2 contour passes with a line offset ($L_o$) of 0.35 mm between them. It then fills the rest of the sample section with a hatch pass with $L_o$ = 0.2 mm.

**Table 1**
Beam parameters in SEBM for the low, medium and high base sinter preheat runs.

| Preheat stages | Base sinter (preheat 1) | | | Local sinter (preheat 2) |
|---|---|---|---|---|
| Accelerating Voltage, $U_e$ (kV) | 60 | | | 60 |
| Beam current, $I_b$ (mA) | 30 | | | 38 |
| Scan velocity, $V_{sc}$ (m $s^{-1}$) | 14.6 | | | 14.6 |
| Line energy, $E_{line}$ (J $m^{-1}$) | 123.3 | | | 156.2 |
| Line offset, $L_0$ (mm) | 1.2 | | | 1.2 |
| Size of the preheat area ($mm^2$) | 190 × 190 | | | Varied |
| Scan repetitions | 2 | 4 | 8 | 1 |
| The applied preheat energy per unit area, $E_A$ (kJ $m^{-2}$) | 206 | 411 | 822 | – |

properties, therefore, this subject requires a better understanding. X-ray computed tomography (XCT) has been widely used in AM for non-destructive metrology [6,15,30] and for product quality assessment [7,30–32]. Here, we examine and elucidate how preheat conditions affect the build quality of AM components using a combination of XCT, image-based modelling, scanning electron microscopy (SEM), and micro-hardness testing.

## 2. Experimental methods

### 2.1. Powder materials

A gas atomised Ti-6Al-4V powder (TLS Technik GmbH & Co. Spezialpulver KG, Germany) was selected for this study owing to its use across a wide range of aerospace and biomedical applications. The Ti-6Al-4V powder morphology was characterised at 20 kV using a SEM (JEOL JSM-6610LV, Japan) in backscattered-electron mode. The powder size distribution (PSD) was determined by a laser diffraction particle size analyzer (Malvern Mastersizer 3000, UK) equipped with a dry dispersion unit.

### 2.2. The selective electron beam melting (SEBM) process

We examined the preheating effects using an Electron Beam Melting A2XX system (Arcam EBM, Sweden) located in the Manufacturing Technology Centre (MTC, UK). The A2XX system operated at a vacuum pressure of $<2 \times 10^{-3}$ mbar and maintained in the vacuum controlled mode. After lowering the stainless steel baseplate, the rake system of the SEBM machine applied a 70 μm thick powder layer on the substrate. Next, the powder layer was preheated and then locally melted by an electron beam. The layer cycle of lowering the build platform, powder raking, preheating and melting was repeated multiple times to build up the components.

As illustrated in Fig. 1, preheating comprises two stages, namely a base sinter and a local sinter, referred to as 'preheat 1' and 'preheat 2' in the ARCAM process, respectively [26]. In the base sinter, the electron beam with an estimated spot size of 800 μm lightly sinters the powder particles over a wide area (Fig. 1a) whereas in the local sinter the electron beam is only scanned across the region of the sample section (Fig. 1b). In ARCAM EBM machines, the preheating temperature is monitored by a K-type thermocouple attached at the bottom of the baseplate which measures the baseplate's temperature rather than the top layer of the powder bed or the AM part and hence this cannot be used to control the process. The target preheat temperature is set to 730 °C (a default ARCAM parameter) [7]. After that, a highly focused electron beam with a spot size of *ca.* 300 μm fuses the sintered Ti-6Al-4V powder together using a default melt scan strategy (illustrated in Fig. 1c). During the melting process, the preheating temperature at the top layer is calculated from the EBM software algorithm (ARCAM A2XX EBM control software ver. 3.2). Lastly, a post-heating stage is applied to the powder bed, maintaining it at high temperature, slowing down the rapid cooling effect, see details in ref. [33]. According to the log file, the electron beam stays on in all processing stages except for powder raking.

In this study, we produced 3 separate SEBM builds; each comprising seven can-shaped samples and a block sample (Fig. 2a) using either 2, 4 or 8 scan repetitions in base sinter (referred to as low, standard and high preheat, respectively). The standard preheating is based on ARCAM A2XX EBM control software ver. 3.2 with the 70 μm theme whereas the others are user modified preheating schemes. The can-shaped sample has an outer diameter of 3 mm, a height of 3 mm and a wall thickness of 1 mm (Fig. 2b). It was designed to preserve the sintered powder (only subjected to the two-stage preheating) from damage during sample handling. Its diameter was set to achieve a high-resolution X-ray computed tomographic analysis. The block sample was 90 mm long ($X$), 14 mm wide ($Y$), and 17 mm tall ($Z$).

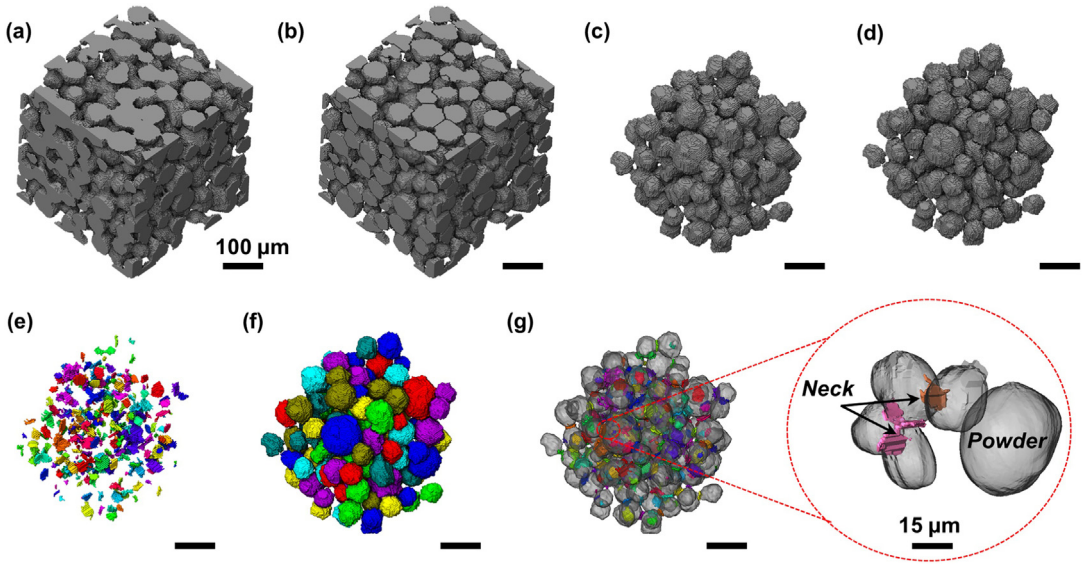


**Fig. 3.** Neck and powder size quantification routine: (a) region of interest (ROI) extracted from the can-shaped sample, and then separated into (b) individual powder particles by the watershed algorithm [36]. *Border kill* function applied on (b) to form (c), powder image. (d) Closing applied on (c) to form the sintered powder image. The sintered neck image formed by (d)–(c), following by connected component analysis to deduce (e) the neck size and (f) powder size; (g) illustrates the sintered necks (coloured) connected with the powder particles (semi-transparent). Scale bars are 100 μm, except in the inset image.

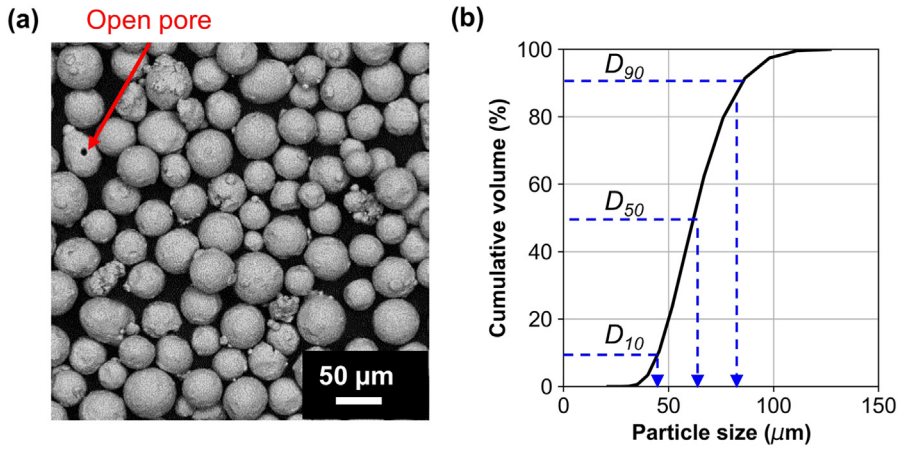


**Fig. 4.** Powder characterisation: (a) backscattered-electron image of Ti-6Al-4V powder showing mostly spherical shaped particles and (b) the PSD measured by laser diffraction analysis.

The SEBM process parameters are summarised in Table 1, wherein the line energy ($E_{line}$) was calculated by $E_{line} = \frac{U_e * I_b}{V_{sc}}$, indicating the applied heat input in SEBM, *i.e.* the higher the $E_{line}$ the higher the heat input. The applied preheat energy per unit area ($E_A$) [26] in base sinter was calculated by: $E_A = \frac{E_{line}}{L_0} * number\ of\ scan\ repetitions$.

### 2.3. Can-shaped samples

#### 2.3.1. X-ray computed tomography (XCT)

All samples were removed from the stainless steel substrate by electrical discharge machining. The can-shaped samples were then scanned by X-ray computed tomography (XCT) to study: 1) the preheating effects on the build accuracy (or build errors) of the additive manufacture (Section 2.3.2.1); 2) the porosity inside the sample wall (Section 2.3.2.2); and 3) the characteristics of the sintered powder bed within the sample (Section 2.3.2.3).

Five out of seven samples for each preheat condition were examined using a *XTH 225* X-ray tomography system (Nikon, Japan) located at the Research Complex at Harwell (RCaH, UK). Each XCT scan was performed at 80 kV and 81 µA, comprising 3142 radiographic projections with a 1 s exposure time per projection. All XCT scans were reconstructed using filtered back projection and beam hardening correction algorithms embedded in CT Pro3D (Nikon, UK). The voxel size of the reconstructed volume is $2.7 \times 2.7 \times 2.7$ µm$^3$.

#### 2.3.2. Image processing and quantification

The reconstructed image volumes were post-processed and quantified by Avizo 7.0 (Thermo Fisher Scientific, USA). Firstly, the input image volume was deblurred by a factor of 3, *i.e.* unsharp masking, for contrast

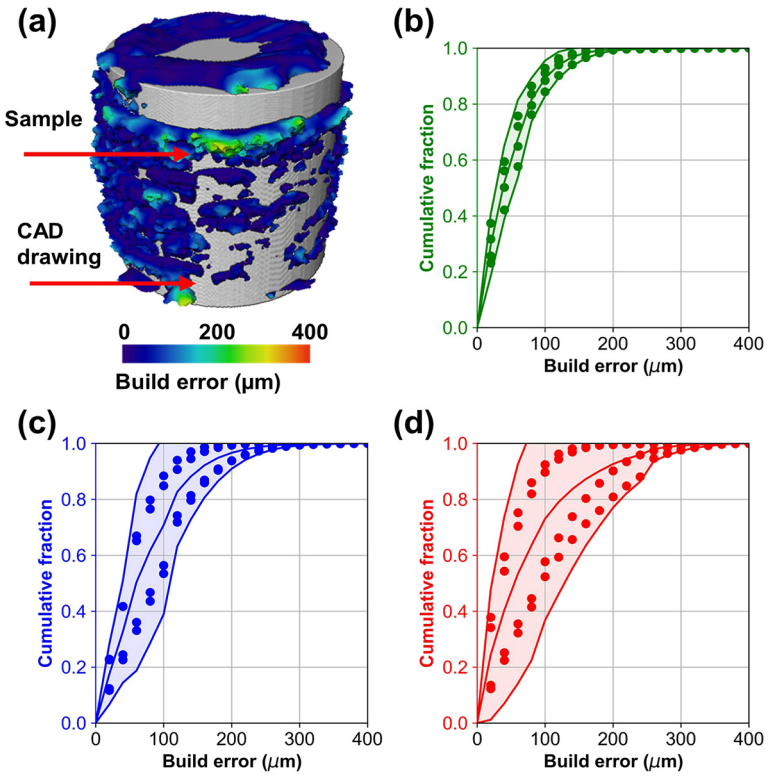


**Fig. 5.** Build errors for SEBM can-shaped samples under different preheat conditions: (a) 3D visualisation of the build error result, where the surface of the reference image (grey) is overlaid with a surface of the can-shaped sample (labelled with a colour map of build errors). The build errors plots for (b) low, (c) standard and (d) high preheat conditions. The shaded region highlights the mean build error ± two standard deviations.

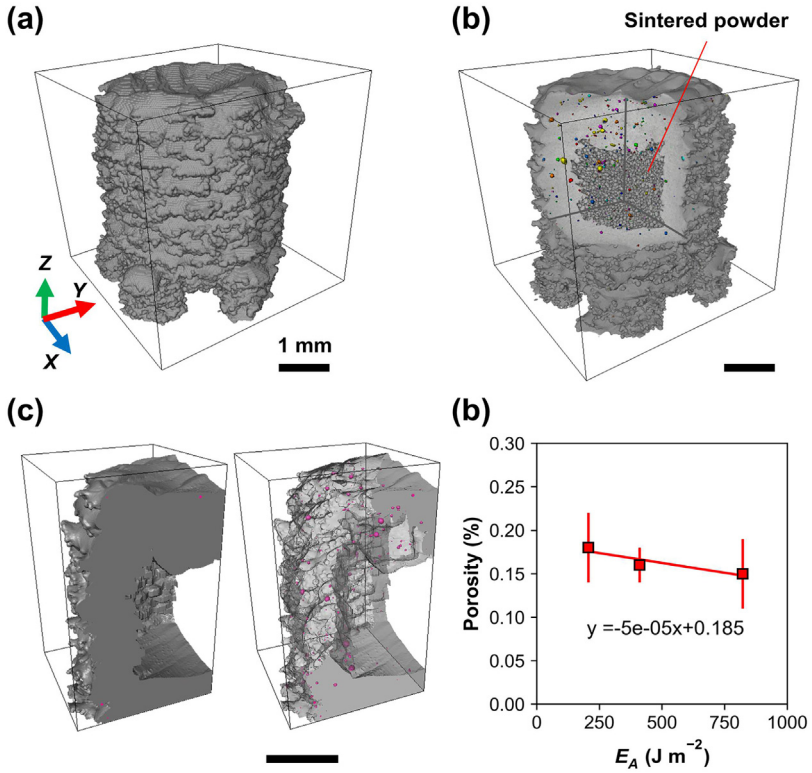


**Fig. 6.** 3D rendered XCT images of the can-shaped sample: (a) external structure, (b) a section view showing sintered powder in the core (grey) and pores (other colours) inside the wall, (c) and a segment showing the pore position in the sample wall (labelled by magenta colour) and (d) the pore fraction analysis.

enhancement and image sharpening. Secondly, a 3D median filter with a kernel of $3 \times 3 \times 3$ was applied to all image volumes for noise removal. Thirdly, the Ti-6Al-4V phase was segmented from the filtered image using the Otsu threshold [34], resulting in a (scanned) binarised image volume.

*2.3.2.1. Quantification of build errors.* To assess the build errors of SEBM components, we imported the CAD drawing of the can-shaped sample into Avizo and segmented it to obtain a reference binary image. A 3D flood-fill operation was applied to the scanned and reference binarised images. After that, we registered the scanned image to the reference image based on the centre of mass. 3D surfaces were then generated for all registered and reference images. Finally, we quantified the build errors by determining the nearest distance between the surfaces of the registered and reference images.

*2.3.2.2. Quantification of porosity.* To quantify the porosity of the can-shaped samples, we applied a boolean negation operator to the threshold images, inverting all the zeros to ones and *vice versa*. We then performed a connected component analysis on the resultant image [35], only accounting for pores located in the sample wall, because only the sample wall underwent preheating and melting.

*2.3.2.3. Quantification of the sintered powder.* We extracted a virtual region of interest (ROI) of $300 \times 300 \times 300$ voxels (equivalent to $0.81 \times 0.81 \times 0.81$ mm$^3$) from the core of the can-shaped samples. We extracted a further one-ninth of the sub-volume to demonstrate the quantification routine (Fig. 3). At first, we performed a connected component analysis on the ROI (Fig. 3a) to obtain the volume fraction of the sintered powder ($\boldsymbol{P_f}$) calculated by dividing the total number of labelled voxels (of the powder) over the total number of voxels in the ROI. Secondly, we separated the sintered powder into individual powder particles (Fig. 3b) using the watershed algorithm [36,37] and then removed any particles that were in contact with the image border using the *border kill* function in Avizo, resulting in a powder image (Fig. 3c). The latter operation was used to reduce the quantification error for subsequent powder size analysis. We then applied a morphological close operation of 1 voxel to re-join the powder particles (Fig. 3d). This was followed by subtracting Fig. 3d from Fig. 3c to obtain an image of the sintered necks. Lastly, we performed a connected component analysis on the sintered neck and powder images to quantify the neck size ($d_{neck}$) (Fig. 3e), powder size ($d_{powder}$) (Fig. 3f), and the neck size ratio, $\boldsymbol{N_r} = \frac{d_{neck}}{d_{powder}}$. The connected component analysis was used to filter out any objects containing <5 voxels to minimise quantification errors [38]. Fig. 3g and the inset show the proposed image quantification routine and the spatial resolution of the XCT scans can effectively quantify the size and shape of the sintered neck between powder particles. We also determined the coordination number of the individual powder particles using an in-house python script, see details in the Supplementary information. The coordination number represents the total number of particles that are in contact with an individual particle. Lastly, we calculated the mean coordination number ($\boldsymbol{C_n}$) for each preheat condition.

**Table 2**
Detail summary of the pore size analysis performed on the solid walls of the can-shaped samples (Fig. 6b).

| Preheat | Pore volume fraction (%) | Mean equivalent diameter (μm) | Max equivalent diameter (μm) | $D_{10}$ (μm) | $D_{50}$ (μm) | $D_{90}$ (μm) |
|---|---|---|---|---|---|---|
| Low | $0.18 \pm 0.04$ | $23 \pm 2$ | 214 | 7 | 18 | 41 |
| Standard | $0.16 \pm 0.02$ | $21 \pm 1$ | 218 | 7 | 17 | 38 |
| High | $0.15 \pm 0.04$ | $21 \pm 1$ | 214 | 7 | 17 | 38 |

**Table 3**
Sinter characteristics and $\lambda_{eff}$ estimated using the Gusarov's approximation [27].

| Preheat | Volume fraction of the sintered powder, $P_f$ | Average coordination number, $C_n$ | Neck size ratio, $N_r$ | Effective thermal conductivity, $\lambda_{eff}$ (W $m^{-1}$ $K^{-1}$) |
|---|---|---|---|---|
| Low | 0.43 ± 0.03 | 4.6 | 0.30 | 1.4 ± 0.2 |
| Standard | 0.48 ± 0.01 | 5.1 | 0.33 | 1.5 ± 0.1 |
| High | 0.47 ± 0.01 | 5.0 | 0.33 | 1.6 ± 0.1 |
| Reference | Simple cubic: 0.52 [45] | 6 | 0–0.3 [45] | 1–2.5 [26] |

### 2.4. Image-based modelling

The beam-matter interaction, melting and solidification in SEBM are governed by the heat transfer mechanism, and hence the effective thermal conductivity $\boldsymbol{\lambda_{eff}}$ of the powder bed. According to Gusarov et al. [27], we can estimate $\boldsymbol{\lambda_{eff}}$:

$$\boldsymbol{\lambda_{eff}} = \boldsymbol{\lambda_{bulk}} \frac{(\boldsymbol{P_f} * \boldsymbol{C_n} * \boldsymbol{N_r})}{\boldsymbol{\pi}}, \quad (1)$$

where the bulk thermal conductivity ($\boldsymbol{\lambda_{bulk}}$) of Ti-6Al-4V at room temperature is ~6.2 W $m^{-1}$ $K^{-1}$, [39] $\boldsymbol{P_f}$, $\boldsymbol{C_n}$, and $\boldsymbol{N_r}$ are dimensionless parameters that describe the morphology of the sintered powder (see details in methods Section 2.3.2.3).

Gusarov et al. [27] considered the dimensionless morphological parameters of the sintered powder, taking into account the average, rather than the local microstructural properties, excluding the effect of thermal diffusivity ($\alpha$) between individual powder particles. To gain a better understanding of the heat transfer mechanism, we performed a heat flux simulation on the sub-volume powder image (*e.g.* Fig. 3a) using an open source application, *TauFactor* [40] in MATLAB (Mathswork Inc., USA). This allowed us to estimate $\tau$ per orthogonal axis as well as along individual powder particles, providing the missing information from the Gusarov's approximation. To simplify our results, we determined the characteristic tau factor ($\tau_c$) by averaging $\tau$ values from all axes, and then calculated the tau factor anisotropy ($\sigma_\tau$) by averaging the sum of squared differences between $\tau_c$ and $\tau$ per orthogonal axis, see details in previous work [41].

The effective thermal diffusivity ($\boldsymbol{\alpha_{eff}}$) could then be calculated by:

$$\boldsymbol{\alpha_{eff}} = \boldsymbol{\alpha_0} \frac{\boldsymbol{\varepsilon}}{\boldsymbol{\tau}} \quad (2)$$

where $\boldsymbol{\alpha_0}$ is the bulk thermal diffusivity and $\boldsymbol{\varepsilon}$ is the porosity. Next, we deduced the $\boldsymbol{\lambda_{eff}}$ by substituting $\boldsymbol{\alpha_{eff}}$ into [26]: $\boldsymbol{\lambda_{eff}} = \boldsymbol{\alpha_{eff}}\, \boldsymbol{\rho}\, \boldsymbol{C_p}$. At room temperature, the bulk thermal diffusivity ($\alpha_0$), density ($\rho$) and heat capacity ($C_p$) of Ti-6Al-4V are 2.9 × $10^{-6}$ $m^2$ $s^{-1}$ [42], 4420 Kg $m^{-3}$ [43], and 546 J $Kg^{-1}$ $K^{-1}$ [43], respectively.

### 2.5. Block samples

#### 2.5.1. Microstructural analysis

The block samples were sectioned into two halves in the *X-Z* direction (Fig. 2a) and polished using SiC discs (P400 to P2400 grits) followed by a 9 μm diamond suspension and then a 0.05 μm silica dioxide suspension, etched by a Kroll reagent for 10 s, and then rinsed in water. They were cleaned with ethanol and dried before SEM imaging. A 2D porosity analysis was performed on the SEM-BS images (0.7 μm per pixel) using ImageJ version 1.51s [44].

#### 2.5.2. Microhardness measurement

We measured the Vickers microhardness (HV 0.5) on the polished surface of the block sample for each preheat condition along the build direction (*Z*) and the transverse direction (*Y*) (denoted in Fig. 2a) using a Buehler MicroMet 6030 hardness tester equipped with a diamond indenter. The microhardness test was performed 2 mm away from the sample edges, covering an area of 10 × 14 mm with 25 indentations.

## 3. Results and discussion

### 3.1. Powder characterisation

The gas atomised Ti-6Al-4V powder is mostly spherical, with a few particles exhibiting open pores and satellites on their surface (Fig. 4a). The powder size distribution (PSD) is in the range of 31–127 μm (Fig. 4b), in which the $D_{10}$, $D_{50}$, and $D_{90}$ are given by 45, 62, and 85 μm, respectively. The size and morphology of the Ti-6Al-4V powder match well with a typical powder used in SEBM [19].

### 3.2. XCT characterisation of the can-shaped samples

#### 3.2.1. Build errors

We used XCT and 3D image processing to quantify the build error of can-shaped samples produced by the three different preheat conditions. Fig. 5a demonstrates a build error map of a can-shaped sample overlaid onto the reference 3D CAD drawing. For each preheat condition, the build error results are collated into a cumulative fraction plot, the lower and upper bounds are two standard deviations from the mean error. The green, blue and red curves correspond to the low (Fig. 5b), standard (Fig. 5c), and high preheating conditions (Fig. 5d). The shaded regions in Fig. 5b–d indicate the process variability of a given preheat condition, the larger the shaded region the more build errors there are. The maximum build error for the low, standard, and high preheat samples are *ca.* 330, 390, and 400 μm, respectively. The results show that there is an increase in build error (*i.e.* a reduction of build accuracy) as $E_A$ increases.

#### 3.2.2. Porosity in the can-shaped samples

The 3D rendered images show the external (Fig. 6a) and internal structures (Fig. 6b) of the can-shaped samples. Fig. 6c illustrates that the porosity analysis was only performed on the walls of the can-shaped samples because the solid walls were subjected to both preheating and melting. Fig. 6d and Table 2 indicate a decrease in the overall porosity of the can-shaped samples, the pore volume, and its size distribution with increasing degree of preheating (or $E_A$). The low preheat samples exhibit the highest pore volume fraction and a pore size distribution with the largest mean pore diameter (Table 2). The standard preheat samples show the lowest standard deviation in the pore volume fraction which indicates the lowest process variability. The high preheat samples exhibit the lowest mean pore volume; however, the large standard deviation value suggests a high degree of preheating cannot be used in isolation to reduce or eliminate defects.

**Table 4**
Tortuosity of the sintered Ti-6Al-4V powder quantified by *TauFactor* [40].

| Preheat | Tortuosity | | | Characteristic tortuosity | Anisotropy of tortuosity | Relative $\sigma_\tau$ (%) |
|---|---|---|---|---|---|---|
| | $\tau_x$ | $\tau_y$ | $\tau_z$ | $\tau_c$ | $\sigma_\tau$ | |
| Low | 3.1 ± 0.3 | 2.9 ± 0.3 | 3.9 ± 0.1 | 3.3 ± 0.2 | 0.78 | 2.2 |
| Standard | 2.8 ± 0.1 | 2.5 ± 0.2 | 3.2 ± 0.3 | 2.9 ± 0.2 | 0.54 | 1.5 |
| High | 2.6 ± 0.1 | 2.6 ± 0.1 | 3.1 ± 0.4 | 2.8 ± 0.2 | 0.35 | 1 |

**Table 5**
The characteristic thermal conductivity ($\lambda_c$) calculated by *Taufactor* [40]. Note: $\lambda_c$ is used interchangeably as $\lambda_{eff}$.

| Preheat | Thermal conductivity (W m$^{-1}$ K$^{-1}$) | | | Characteristic thermal conductivity (W m$^{-1}$ K$^{-1}$) |
|---|---|---|---|---|
| | $\lambda_x$ | $\lambda_y$ | $\lambda_z$ | $\lambda_c$ |
| Low | 1.36 ± 0.18 | 1.45 ± 0.14 | 1.07 ± 0.04 | 1.27 ± 0.10 |
| Standard | 1.38 ± 0.10 | 1.53 ± 0.12 | 1.20 ± 0.06 | 1.35 ± 0.04 |
| High | 1.50 ± 0.07 | 1.50 ± 0.07 | 1.30 ± 0.14 | 1.43 ± 0.07 |

*3.2.3. The effective thermal conductivity of the powder bed*

The effective thermal conductivity ($\lambda_{eff}$) of the sintered Ti-6Al-4V powder was calculated by two image-based modelling methods, namely; (1) using the Gusarov's approximation [27] and (2) using the heat flux simulation [40]. Table 3 displays dimensionless morphological parameters of the sintered characteristics and the $\lambda_{eff}$ of the powder bed. The neck size ratio, $N_r$, is a measurement of how well particles are sintered together, *i.e.* the larger the $N_r$ the better the particles are sintered. $N_r$ is found to be in the range of 0.30–0.33 across all samples and slightly above the predicted $N_r$ for laser powder bed fusion (LPBF), *e.g.* 0–0.3 [45]. Larger $N_r$ values are found in SEBM compared to LBPF because (1) SEBM has a longer preheating time (*e.g.* seconds) compared to that in LPBF (*e.g.* milliseconds) and (2) it uses twice the powder size of that in LPBF [12]. The $N_r$ is closely linked to the volume fraction of the sintered powder, $P_f$, because preheating promotes partial melting at the powder surfaces *via* liquid phase sintering [46] which involves grain arrangement, formation and densification of the solid skeletal network (or sintered powder), so that this increases the $P_f$ whilst reducing the porosity of the sintered structure. Our calculated $P_f$ values (0.43–0.48) match well with the value of <0.5 hypothesised by Körner et al. [47]. The average coordination number, $C_n$, is very similar for both standard and high preheat conditions and slightly larger than the low preheat condition. It indicates that the number of particles that are in contact with each other did not increase beyond standard preheating, however, the mean $\lambda_{eff}$ of the powder bed continues to increase with increasing $E_A$. Given that the standard deviation of $\lambda_{eff}$ is relatively large, more evidence is required to confirm whether the calculated $\lambda_{eff}$ is statistically significant.

The heat flux simulation results show that the anisotropy of tortuosity, $\sigma_\tau$, reduces from 0.78 to 0.35 (Table 4) and increases the characteristic thermal conductivity, $\tau_c$, gradually from 1.27 ± 0.10 to 1.43 ± 0.07 W m$^{-1}$ K$^{-1}$ (Table 5) with an increasing number of scan repetitions (or $E_A$) in the base sinter (preheat 1). This demonstrates that the structure of the sintered powder becomes more isotropic with a higher degree of preheating and the thermal conductivity is *ca.* 30%, 20%, and 10% lower in the *Z* build direction compared to the lateral *X* or *Y* direction for low, standard, and high preheats, respectively, *i.e.* $\lambda_z < \lambda_x \cong \lambda_y$. Our 3D quantification results confirm that the sintered powder bed exhibits an anisotropic microstructure and also demonstrate that a high degree of preheating can reduce the microstructural anisotropy, promoting heat transfer for processing stages. We speculate that the microstructural anisotropy may be caused by the preferential electron beam-powder (or beam-matter) interaction near the powder bed surface wherein neck formation occurs at the powder bed surface rather than between powder layers. With a low $\lambda_z$, the contact area between powder layers is expected to be small (Table 3), leading to an inefficient beam-matter interaction, including local preheating and melting processes, [21] promoting defect formation (Table 2). The impact of preheating on microstructural and mechanical properties of AM components will be discussed further in the next section.

The value of $\lambda_{eff}$ estimated by the heat flux simulation shows a much lower standard deviation (Table 5) than that predicted by the Gusarov approximation (Table 3), because the heat flux simulation takes the local variations of the microstructure into account whereas the Gusarov approximation is based on the bulk microstructural characteristics. Therefore, the heat flux simulation predictions are somewhat more precise than the Gusarov approximation. Given that both image-based modelling results are of the same order of magnitude, this suggests that the increase of $\lambda_{eff}$ with increasing scan repetitions is statistically significant.

Here, we compare the effects of the base sinter or preheat 1 (current study) and the local sinter or preheat 2 (Smith et al. [26]) on the $\lambda_{eff}$ of the powder bed, see Fig. 7, given that both studies used the same set of beam parameters, including $U_E$, $I_b$, $v_{sc}$, and $L_0$. The estimated $\lambda_{eff}$ values from Tables 3 and 5 are in the same order of magnitude as those obtained from a laser flash experiment by Smith et al. [26] (Fig. 7), suggesting that image-based modelling combined with XCT quantification analysis is a reliable alternative method to deduce $\lambda_{eff}$. Moreover, our results reveal and quantify, for the first time, the thermal properties of the powder bed in 3D.

Fig. 7 shows that $\lambda_{eff}$ increases linearly with the base sinter energy $E_A$ but it increases non-linearly with $E_A$ in the local sinter [26]. This suggests that $\lambda_{eff}$ is not only affected by $E_A$ but is also affected by other process parameters in SEBM. The calculated $\lambda_{eff}$ from Smith et al. [26] study is much lower than our results because the base sinter's preheat area in the current study is *ca.* 10% smaller than that used in their work, resulting in a higher $\lambda_{eff}$, *i.e.* the $\lambda_{eff}$ is affected more by reducing the preheat area in base sinter, rather than by increasing scan repetitions in base sinter.

When the critical $E_A$ is below 500 kJ m$^{-2}$ (based on the heat flux simulation) or 625 kJ m$^{-2}$ (based on Gusarov approximation), the

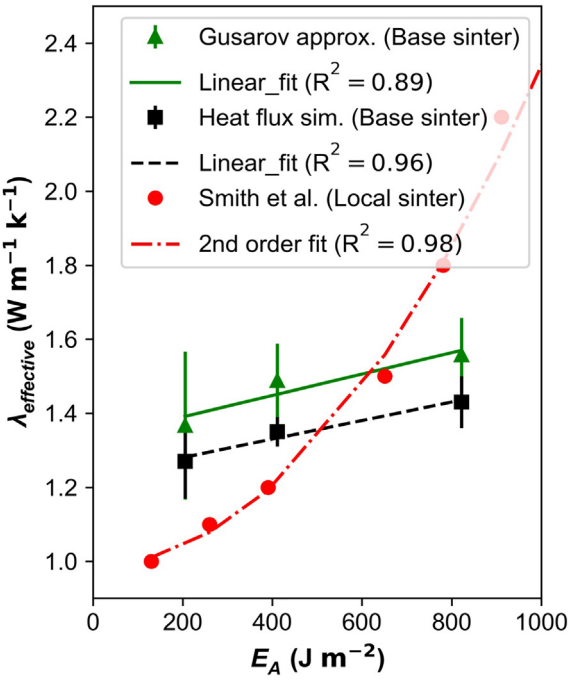


**Fig. 7.** The influence of applied preheat energy per unit area ($E_A$) on the effective thermal conductivity ($\lambda_{eff}$). The vertical line shows the data points when both studies use the same base sinter setting ($E_A$ = 411 kJ m$^{-2}$). Corresponding lines of best fit for Gusarov approximation ($y = -2.9x + 1.3$) and for the heat flux simulation ($y = -2.5x + 1.2$) are in green and black colours, respectively.

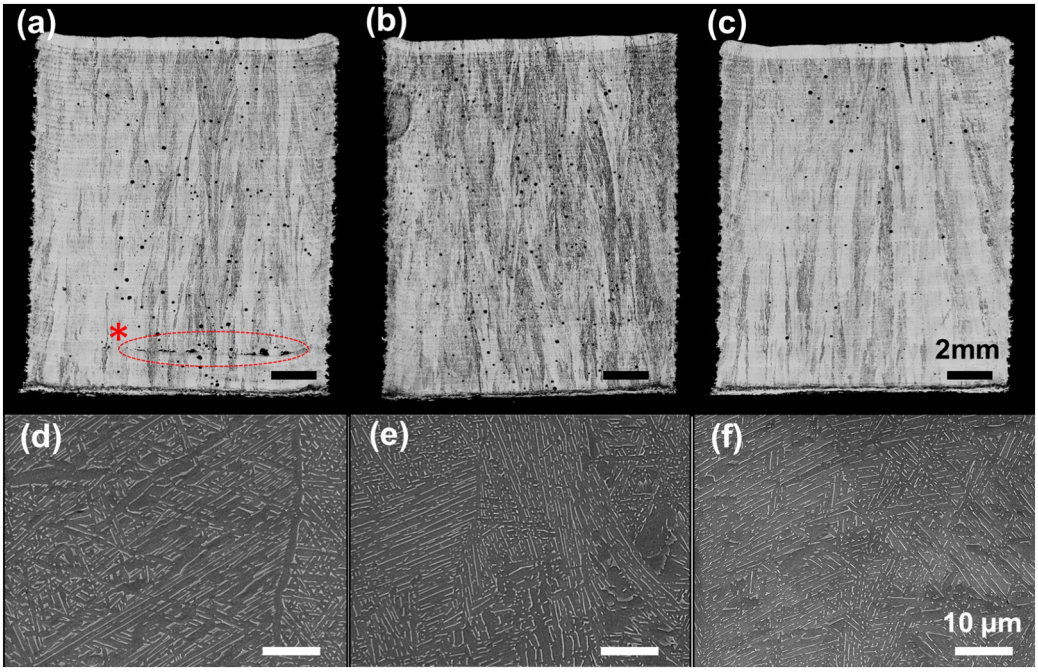


**Fig. 8.** Example of etched micrographs from the block samples along the *Y-Z* plane produced by (a) low, (b) standard, and (c) high preheating conditions in mm scale (top row). High-resolution SEM images of (d) low, (e) standard, and (f) high preheat sample at 2000× magnification. The red asterisk shows the position of the lack of fusion defect.

reduction in preheat area combined with increasing scan repetitions in base sinter is a major contributor to the increase of $\lambda_{eff}$. Once $E_A$ exceeds the critical value, additional scan repetitions in base sinter would have a negligible effect on $\lambda_{eff}$ whereas the increase of scan repetitions in local sinter will become a dominant factor for the increase of $\lambda_{eff}$.

### 3.3. Microstructural properties of the block samples

SEM was used to investigate the effects of preheating on the microstructure of the block samples. Fig. 8 shows that all three block samples exhibit large columnar prior beta grains along the (*Z*) build direction. Fig. 8a shows that the low preheat sample contains spherical pores and lack of fusion defects near the lower part of the sample (see the red circle and Supplementary Fig. 3). However, the standard (Fig. 8b) and high preheat (Fig. 8c) samples only exhibit spherical pores. Since SEBM AM is undertaken under vacuum, these spherical pores may be formed due to the release of gas from the gas atomised powder during SEBM [7] whereas lack of fusion defects may be formed due to a low $P_f$ (or low $\lambda_{eff}$) in the powder bed [48].

Based on 2D image analysis, the porosity area (%) of low, standard and high preheat samples are 0.58 ± 0.4% to 0.57 ± 0.3%, and 0.57 ± 0.3%, respectively. These results show a relatively high standard deviation across all samples, suggesting that an increasing number of scan repetitions or $E_A$ in base sinter has a negligible effect on porosity in large SEBM samples.

Given that all the samples were held at, or above, the preheat temperature during preheating and melting, we speculate that all samples cool slowly, resulting in Widmanstätten lath-like α phase within a

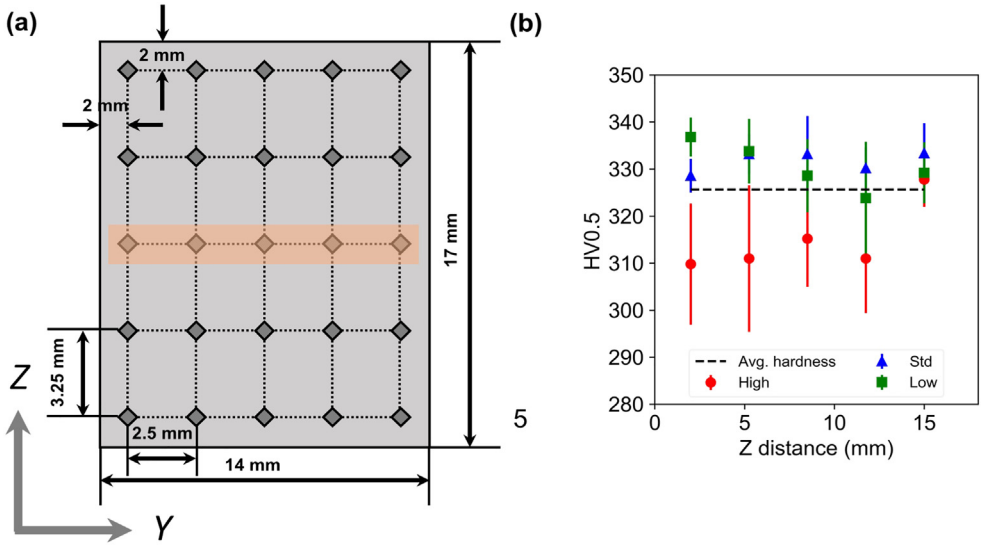


**Fig. 9.** The hardness measurements on three block samples in the *Y-Z* plane: (a) an illustration of the indentation position of the block sample wherein the orange region shows that the mean and standard deviation of the microhardness will be calculated in the *Y* direction; (b) shows the corresponding microhardness plot along the *Z* distance.

matrix of $\beta$ and limiting the possibility of forming $\alpha''$-martensite [49] (Fig. 8d–f).

### 3.4. Mechanical properties of the block samples

We performed microhardness tests on one fully consolidated block sample for each preheat condition to investigate the effects of preheating on their local mechanical properties in the *Y-Z* plane, denoted by Fig. 2a. Fig. 9a illustrates the indentation positions on the *Y-Z* plane of the block sample. The mean and standard deviation of the microhardness values of the Ti-6Al-4V block samples are calculated along the *Y* direction (highlighted in orange - Fig. 9a) and then plotted against with various *Z* height (Fig. 9b). The low, standard, and high preheat samples have a microhardness of 330 ± 7, 332 ± 5, and 315 ± 11 Hv0.5, respectively.

Fig. 9b shows that the high preheat samples exhibit anisotropic mechanical properties and their microhardness is *ca.* 10% lower than other block samples (except for the measurements at $Z = 15$ mm). This is because the high preheat block samples were maintained at 730 °C for at least twice the preheat time compared to the other block samples, *i.e.* subjected to longer annealing. Their microstructure is expected to coarsen [50], forming large α lathes, resulting in a low microhardness. In contrast, a sudden increase in microhardness at *Z* from 12.5 to 15 mm is possibly owing to the fact that the top segment underwent a shorter annealing cycle than the lower segment and a slightly higher cooling rate, resulting in a fine grain microstructure with a high hardness value [49,50]. Our results suggest the high preheat samples exhibit a coarse-to-fine microstructure along the *Z* build direction [51]. Lastly, all samples seemed to exhibit a similar microhardness at $Z = 15$ mm presumably because there is insufficient annealing to have an effect on the microstructure.

## 4. Conclusions

We have investigated the material-process-structure-property relationships in SEBM by varying the number of scan repetitions or preheat energy per unit area ($E_A$) in base sinter (Preheat 1). The key conclusions from this study are as follows:

1) X-ray Computed Tomography (XCT) was employed to quantify the sintered characteristics of the powder bed, including neck size ratio, packing fraction, and coordination number, under three different preheating strategies. The results reveal that the sintered powder bed exhibits an anisotropic microstructure and show that base sinter preheating is sufficient to promote powder sintering for SEBM.
2) The tortuosity and effective thermal conductivity ($\boldsymbol{\lambda_{eff}}$) of the sintered powder bed were calculated by heat flux simulation and numerical models using XCT and image-based modelling. Our results show that $\boldsymbol{\lambda_{eff}}$ increases with increasing $E_A$ and decreasing the size of the build chamber. Under the conditions studied, the thermal conductivity along the build height ($\boldsymbol{\lambda_z}$) is always higher than that in other directions, *i.e.* $\boldsymbol{\lambda_x \cong \lambda_y < \lambda_z}$. The anisotropy in thermal conductivity can be reduced by increasing $E_A$ due to an increase in powder densification.
3) Prolonged preheating has a minimal effect on the porosity of the SEBM components, however, under the conditions studied it reduces the precision and accuracy of the SEBM process. The maximum build error increases from 330 to 400 μm with increasing $E_A$.
4) The microhardness of the SEBM components falls slightly from 330 ± 7 to 315 ± 11 HV0.5 with increasing $E_A$ due to microstructural coarsening of Ti-6Al-4V *via* annealing which can be accelerated by increasing $E_A$ and preheating time. The reduction of hardness is more apparent in the lower segment of the high preheat samples.
5) A medium $E_A$ (411 kJ $m^{-2}$) was found to be the optimum preheat condition, producing components with a high hardness and moderate build accuracy. There are other benefits in selecting an optimum preheating strategy, including reduction of the overall build time and less powder being sintered which improves the powder recyclability.

## Acknowledgments

The authors acknowledge financial support from the EPSRC MAPP Future Manufacturing Hub (EP/P006566/1, www.mapp.ac.uk) and grants (EP/I02249X/1 and EP/M009688/1) and the AMAZE (Additive Manufacturing Aiming towards Zero Waste and Efficient Production of High-Tech Metal Products) project funded by the 7th Framework Programme of the European Commission (contract FP7-2012-NMP-ICT-FoF-313781). We acknowledge the use of facilities and support provided by the Research Complex at Harwell. PJW is grateful for funding from the ERC Advanced Grant (CORREL-CT Project ID: 695638).

## Author contributions

CLAL, PDL, RT, and EM conceived the project. CLAL and SN performed the XCT experiments. CLAL performed the XCT analysis, numerical and heat flux simulation, data analysis, and result interpretation. RT and EM produced the samples. RT performed metallography and hardness testing. CLAL, PDL, and PJW led the results interpretation and paper writing, with all authors contributing.

## Data availability

Representative samples of the research data are given in the figures (and Supplementary data – DOI if available). Other datasets generated and/or analysed during this study are not publicly available due to their large size but are available from the corresponding author on reasonable request.

## Competing interests

The authors declare no competing financial interests.

## Appendix A. Supplementary data

Supplementary data to this article can be found online at https://doi.org/10.1016/j.matdes.2019.107792.

## References

[1] L.C. Zhang, Y. Liu, S. Li, Y. Hao, Additive manufacturing of titanium alloys by electron beam melting: a review, Adv. Eng. Mater. 20 (2018)https://doi.org/10.1002/adem.201700842.
[2] A. Pramanik, Problems and solutions in machining of titanium alloys, Int. J. Adv. Manuf. Technol. 70 (2014) 919–928, https://doi.org/10.1007/s00170-013-5326-x.
[3] I. Gibson, D.W. Rosen, B.E. Stucker, D.B.S. Dr. Ian Gibson, Dr. David W. Rosen, Additive Manufacturing Technologies, 1st ed., Springer New York, London, 2010.
[4] ASTM F42.91, F2792-12a: Standard Terminology for Additive Manufacturing Technologies, ASTM Int., 2012 1–3, https://doi.org/10.1520/F2792-12A.
[5] R.J. Moat, A.J. Pinkerton, L. Li, P.J. Withers, M. Preuss, Residual stresses isn laser direct metal deposited Waspaloy, Mater. Sci. Eng. A 528 (2011) 2288–2298, https://doi.org/10.1016/j.msea.2010.12.010.
[6] T.B. Kim, S. Yue, Z. Zhang, E. Jones, J.R. Jones, P.D. Lee, Additive manufactured porous titanium structures: through-process quantification of pore and strut networks, J. Mater. Process. Technol. 214 (2014) 2706–2715, https://doi.org/10.1016/j.jmatprotec.2014.05.006.
[7] S. Tammas-Williams, H. Zhao, F. Léonard, F. Derguti, I. Todd, P.B. Prangnell, XCT analysis of the influence of melt strategies on defect population in Ti-6Al-4V components manufactured by selective electron beam melting, Mater. Charact. 102 (2015) 47–61, https://doi.org/10.1016/j.matchar.2015.02.008.
[8] Y. Liu, Y. Yang, S. Mai, D. Wang, C. Song, Investigation into spatter behavior during selective laser melting of AISI 316L stainless steel powder, Mater. Des. 87 (2015) 797–806, https://doi.org/10.1016/j.matdes.2015.08.086.
[9] D. Wang, S. Wu, F. Fu, S. Mai, Y. Yang, Y. Liu, C. Song, Mechanisms and characteristics of spatter generation in SLM processing and its effect on the properties, Mater. Des. 117 (2017) 121–130, https://doi.org/10.1016/j.matdes.2016.12.060.
[10] C.L.A. Leung, S. Marussi, M. Towrie, J. del Val Garcia, R.C. Atwood, A.J. Bodey, J.R. Jones, P.J. Withers, P.D. Lee, Laser-Matter Interactions in Additive Manufacturing

of Stainless Steel SS316L and 13–93 Bioactive Glass Revealed by In Situ X-Ray Imaging, Elsevier, 2018https://www.sciencedirect.com/science/article/pii/S2214860418303178, Accessed date: 9 January 2019.
[11] C.L.A. Leung, S. Marussi, M. Towrie, R.C. Atwood, P.J. Withers, P.D. Lee, The effect of powder oxidation on defect formation in laser additive manufacturing, Acta Mater. 166 (2019) 294–305, https://doi.org/10.1016/J.ACTAMAT.2018.12.027.
[12] C.L.A. Leung, S. Marussi, R.C. Atwood, M. Towrie, P.J. Withers, P.D. Lee, In situ X-ray imaging of defect and molten pool dynamics in laser additive manufacturing, Nat. Commun. 9 (2018), 1355. https://doi.org/10.1038/s41467-018-03734-7.
[13] Y. Kok, X.P. Tan, P. Wang, M.L.S. Nai, N.H. Loh, E. Liu, S.B. Tor, Anisotropy and heterogeneity of microstructure and mechanical properties in metal additive manufacturing: a critical review, Mater. Des. 139 (2018) 565–586, https://doi.org/10.1016/J.MATDES.2017.11.021.
[14] W.E. Frazier, Metal additive manufacturing: a review, J. Mater. Eng. Perform. 23 (2014) 1917–1928, https://doi.org/10.1007/s11665-014-0958-z.
[15] C.J. Smith, F. Derguti, E. Hernandez Nava, M. Thomas, S. Tammas-Williams, S. Gulizia, D. Fraser, I. Todd, Dimensional accuracy of Electron Beam Melting (EBM) additive manufacture with regard to weight optimized truss structures, J. Mater. Process. Technol. 229 (2016) 128–138, https://doi.org/10.1016/j.jmatprotec.2015.08.028.
[16] M. Todai, T. Nakano, T. Liu, H.Y. Yasuda, K. Hagihara, K. Cho, M. Ueda, M. Takeyama, Effect of building direction on the microstructure and tensile properties of Ti-48Al-2Cr-2Nb alloy additively manufactured by electron beam melting, Addit. Manuf. 13 (2017) 61–70, https://doi.org/10.1016/j.addma.2016.11.001.
[17] H. Weiwei, J. Wenpeng, L. Haiyan, T. Huiping, K. Xinting, H. Yu, Research on preheating of titanium alloy powder in electron beam melting technology, Rare Met. Mater. Eng. 40 (2011) 2072–2075, https://doi.org/10.1016/S1875-5372(12)60014-9.
[18] C.K. T. Scharowsky, A. Bauereiß, R.F. Singer, Observation and numerical simulation of melt pool dynamic and beam powder interaction during selective electron beam melting, FFF Work. (2012) 815–820. http://internal-pdf//Observation and numerical simulation of melt pool dynamic a-2533632288/Observation and numerical simulation of melt pool dynamic and beam powder interaction during selective electron beam melting.pdf.
[19] C. Körner, Additive manufacturing of metallic components by selective electron beam melting — a review, Int. Mater. Rev. 61 (2016) 361–377, https://doi.org/10.1080/09506608.2016.1176289.
[20] D. Cormier, O. Harrysson, H. West, Characterization of H13 steel produced via electron beam melting, Rapid Prototyp. J. 10 (2004) 35–41, https://doi.org/10.1108/13552540410512516.
[21] M. Kahnert, S. Lutzmann, M. Zäh, Layer formations in electron beam sintering, in: Solid Free Form Fabr. Symp., 2007: pp. 88–99. http://edge.rit.edu/content/P10551/public/SFF/SFF 2007 Proceedings/Manuscripts/08-Kahnert.pdf.
[22] M. Sigl, S. Lutzmann, M.F. Zäh, Transient physical effects in electron beam sintering, Solid Free. Fabr. Proc. 2006, pp. 464–477.
[23] J. Milberg, M. Sigl, Electron beam sintering of metal powder, Prod. Eng. 2 (2008) 117–122.
[24] H.B. Qi, Y.N. Yan, F. Lin, W. He, R.J. Zhang, Direct metal part forming of 316L stainless steel powder by electron beam selective melting, Proc. Inst. Mech. Eng. Part B J. Eng. Manuf. 220 (2006) 1845–1853.
[25] X. Gong, K. Chou, Characterization of sintered Ti-6Al-4V powders in Electron beam additive manufacturing, in: Proc. ASME 2013 Int. Manuf. Sci. Eng. Conf., American Society of Mechanical Engineers, 2013: p. V001T01A002-V001T01A002.
[26] C.J. Smith, S. Tammas-Williams, E. Hernandez-Nava, I. Todd, Tailoring the thermal conductivity of the powder bed in Electron Beam Melting (EBM) additive manufacturing, Sci. Rep. 7 (2017), 10514. https://doi.org/10.1038/s41598-017-11243-8.
[27] A.V. Gusarov, T. Laoui, L. Froyen, V.I. Titov, Contact thermal conductivity of a powder bed in selective laser sintering, Int. J. Heat Mass Transf. 46 (2003) 1103–1109, https://doi.org/10.1016/S0017-9310(02)00370-8.
[28] M.F. Zäh, S. Lutzmann, M. Kahnert, F. Walchshäusl, Determination of process parameters for Electron beam sintering (EBS), Proc. COMSOL Conf. 2008, Hannover, 2008.
[29] E. Rodriguez, F. Medina, D. Espalin, C. Terrazas, D. Muse, C. Henry, E. MacDonald, R.B. Wicker, Integration of a thermal imaging feedback control system in electron beam melting, Proc. Solid Free. Fabr. Symp, 2012.
[30] C. Qiu, S. Yue, N.J.E. Adkins, M. Ward, H. Hassanin, P.D. Lee, P.J. Withers, M.M. Attallah, Influence of processing conditions on strut structure and compressive properties of cellular lattice structures fabricated by selective laser melting, Mater. Sci. Eng. A 628 (2015) 188–197, https://doi.org/10.1016/j.msea.2015.01.031.
[31] S. Tammas-Williams, P.J. Withers, I. Todd, P.B. Prangnell, The effectiveness of hot isostatic pressing for closing porosity in titanium parts manufactured by selective electron beam melting, Metall. Mater. Trans. A Phys. Metall. Mater. Sci. 47 (2016) 1939–1946, https://doi.org/10.1007/s11661-016-3429-3.
[32] Z. Zhang, D. Jones, S. Yue, P.D. Lee, J.R. Jones, C.J. Sutcliffe, E. Jones, Hierarchical tailoring of strut architecture to control permeability of additive manufactured titanium implants, Mater. Sci. Eng. C. 33 (2013) 4055–4062, https://doi.org/10.1016/j.msec.2013.05.050.
[33] W. Sames, Additive Manufacturing of Inconel 718 Using Electron Beam Melting: Processing, Post-Processing, &Amp; Mechanical Properties, https://oaktrust.library.tamu.edu/handle/1969.1/155230 2015, Accessed date: 21 January 2019.
[34] N. Otsu, A threshold selection method from gray-level histograms, IEEE Trans. Syst. Man. Cybern. 9 (1979) 62–66, https://doi.org/10.1109/TSMC.1979.4310076.
[35] L. He, X. Ren, Q. Gao, X. Zhao, B. Yao, Y. Chao, The connected-component labeling problem: a review of state-of-the-art algorithms, Pattern Recogn. 70 (2017) 25–43, https://doi.org/10.1016/J.PATCOG.2017.04.018.
[36] S. Yue, P.D. Lee, G. Poologasundarampillai, J.R. Jones, Evaluation of 3-D bioactive glass scaffolds dissolution in a perfusion flow system with X-ray microtomography, Acta Biomater. 7 (2011) 2637–2643, https://doi.org/10.1016/j.actbio.2011.02.009.
[37] R.C. Atwood, J.R. Jones, P.D. Lee, L.L. Hench, Analysis of pore interconnectivity in bioactive glass foams using X-ray microtomography, Scr. Mater. 51 (2004) 1029–1033, https://doi.org/10.1016/J.SCRIPTAMAT.2004.08.014.
[38] E. Maire, P.J. Withers, Quantitative X-ray tomography, Int. Mater. Rev. 59 (2014) 1–43, https://doi.org/10.1179/1743280413Y.0000000023.
[39] X. Gong, B. Cheng, S. Price, K. Chou, Powder-bed electron-beam-melting additive manufacturing: Powder characterization, process simulation and metrology, Proc. ASME Dist. F Early Career Tech. Conf 2013, pp. 59–66.
[40] S.J. Cooper, A. Bertei, P.R. Shearing, J.A. Kilner, N.P. Brandon, TauFactor: an open-source application for calculating tortuosity factors from tomographic data, SoftwareX 5 (2016) 203–210, https://doi.org/10.1016/J.SOFTX.2016.09.002.
[41] S.J. Cooper, D.S. Eastwood, J. Gelb, G. Damblanc, D.J.L. Brett, R.S. Bradley, P.J. Withers, P.D. Lee, A.J. Marquis, N.P. Brandon, P.R. Shearing, Image based modelling of microstructural heterogeneity in $LiFePO_4$ electrodes for Li-ion batteries, J. Power Sources 247 (2014) 1033–1039, https://doi.org/10.1016/j.jpowsour.2013.04.156.
[42] S. Draper, B. Lerch, R. Rogers, R. Martin, I. Locci, A. Garg, Materials characterization of electron beam melted Ti-6Al-4V, Proc. 13th World Conf. Titan, John Wiley & Sons, Inc, Hoboken, NJ, USA 2016, pp. 1433–1440, https://doi.org/10.1002/9781119296126.ch242.
[43] J.J. Valencia, P.N. Quested, Thermophysical properties, ASM Handb. Cast. 15 (2008) 468–481, https://doi.org/10.1361/asmhba0005240.
[44] C. Schneider, W.S. Rasband, K.W. Eliceiri, NIH image to ImageJ: 25 years of image analysis, Nat. Methods 9 (2012) 671–675, https://doi.org/10.1038/nmeth.2089.
[45] A.V. Gusarov, I. Smurov, Modeling the interaction of laser radiation with powder bed at selective laser melting, 6th Int. Conf. Laser Assist. Net Shape Eng. LANE 2010, Sept. 21, 2010 - Sept. 24, 2010, vol. 5, 2010, pp. 381–394, https://doi.org/10.1016/j.phpro.2010.08.065.
[46] R.M. German, P. Suri, S.J. Park, Review: liquid phase sintering, J. Mater. Sci. 44 (2009) 1–39, https://doi.org/10.1007/s10853-008-3008-0.
[47] C. Körner, A. Bauereiß, E. Attar, Fundamental consolidation mechanisms during selective beam melting of powders, Model. Simul. Mater. Sci. Eng. 21 (2013), 085011. https://doi.org/10.1088/0965-0393/21/8/085011.
[48] E. Attar, Simulation of Selective Electron Beam Melting Processes, Uniersity of Erlangen, 2011.
[49] J. Tong, C.R. Bowen, J. Persson, A. Plummer, Mechanical properties of titanium-based Ti–6Al–4V alloys manufactured by powder bed additive manufacture, Mater. Sci. Technol. (United Kingdom). 33 (2017) 138–148, https://doi.org/10.1080/02670836.2016.1172787.
[50] S.S. Al-Bermani, M.L. Blackmore, W. Zhang, I. Todd, The origin of microstructural diversity, texture, and mechanical properties in electron beam melted Ti-6Al-4V, Metall. Mater. Trans. A Phys. Metall. Mater. Sci. 41 (2010) 3422–3434, https://doi.org/10.1007/s11661-010-0397-x.
[51] S.L. Lu, H.P. Tang, Y.P. Ning, N. Liu, D.H. StJohn, M. Qian, Microstructure and mechanical properties of long Ti-6Al-4V rods additively manufactured by selective Electron beam melting out of a deep powder bed and the effect of subsequent hot isostatic pressing, Metall. Mater. Trans. A. 46 (2015) 3824–3834, https://doi.org/10.1007/s11661-015-2976-3.